

REGIONAL AND HISTORICAL GEOCRYOLOGY

DOI: 10.21782/EC2541-9994-2019-3(3-10)

ELECTRICAL RESISTIVITY TOMOGRAPHY FOR IDENTIFICATION OF FROZEN AND COLD SALINE ROCKS

D.A. Kvon¹, I.N. Modin², V.A. Shevnin², D.V. Makarov², A.D. Skobelev^{1,2}¹Research Center Geoscan LLC, 95, Leninsky prosp., Moscow, 119313, Russia; kvonchik@rambler.ru²Lomonosov Moscow State University, Faculty of Geology, 1, Leninskie Gory, Moscow, 119991, Russia

Shallow subsurface in the permafrost zone around the Kharasavei gas and condensate field in the Yamal Peninsula is studied by electrical resistivity tomography (ERT) to characterize the thermal state and salinity of the ground. Resistivity patterns obtained by statistical processing of ERT data jointly with petrophysical modeling allow discriminating between deposits of different salinities and imaging the section structure. A procedure is suggested to estimate pore fluid salinity from resistivity data.

Electrical resistivity tomography, petrophysical modeling, saline permafrost, cold ground

INTRODUCTION

The Kharasavei gas and condensate field is located in the zone of continuous permafrost [Badu and Podbornyi, 2006] with widespread saline and cold soils [Budantseva et al., 2006].

The salinity of pore fluids affects their freezing temperature and phase state and, as a result, the mechanical properties of frozen ground. Salinity of soils in the Kharasavei field poses major risks to the operation of wells and production-related facilities [Budantseva et al., 2006].

The shallow permafrost structure has been often imaged lately by electrical resistivity tomography (ERT) which provides high-resolution and high-quality data. ERT results were reported from highland permafrost areas [Hauck, 2002; Krautblatter et al., 2010] and from the Arctic coast [Yoshikawa et al., 2006; Hubbard et al., 2013; Olenchenko et al., 2015]. Yet, there are few examples of ERT surveys in saline permafrost [Ingeman-Nielsen et al., 2008; Dafflon et al., 2016] with implications to the amount of unfrozen pore water [Oldenborger, LeBlanc, 2017].

We present ERT data from several sites in the northwestern Yamal Peninsula within the Kharasavei gas and condensate field which reveal the structure, thermal state, and pore fluid salinity patterns of shallow subsurface.

Geomorphological and geological background

The sites of ERT surveys and boundaries of geological and geomorphological units [Podbornyi, 2006] are shown in the map of Fig. 1. Two sites are located within the marine terrace mIII₂₋₃, at elevations of 20–22 m above sea level. According to drilling evi-

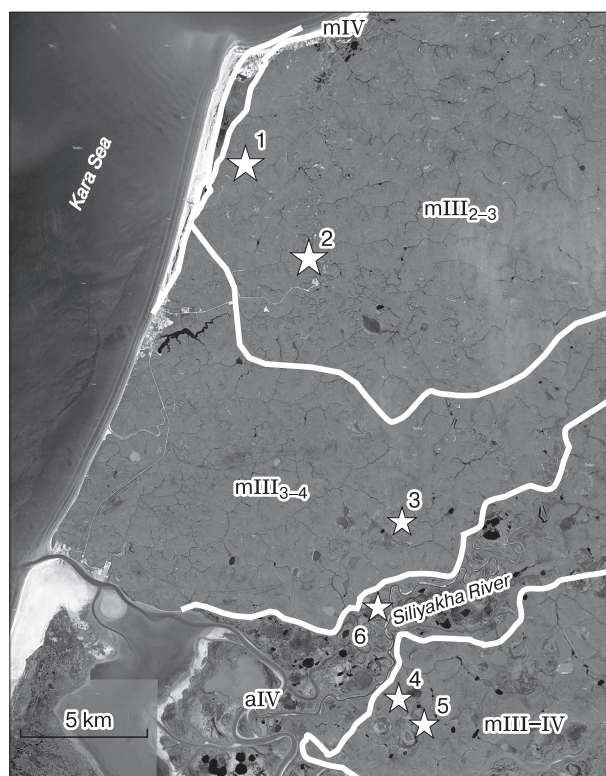


Fig. 1. Map of study area with elements of geomorphology.

1–6 = survey sites. Upper Quaternary marine sediments (clay silt, clay, sand and silt): mIII₂₋₃ = terrace III, 20–22 m asl; mIII₃₋₄ = terrace II, 12 m asl; mIII–IV = terrace I, Holocene, 10–12 m asl. Holocene sediments: mIV = laid marine deposits (sand, clay silt, clay); aIV = floodplain alluvium (sand, peaty silt).

dence from site 1, the section consists of (top to bottom) clay silt with lens-like and layered cryostructures (10–12 m); massive sand (12 to 30 m); and massive clay silt (30 to at least 50 m). The section of site 2 is likewise composed of clay silt with lens-type and layered cryostructures (upper 10 m), massive sand (between 10 and 35 m), and massive clay silt interbedded with silt from 35 to 50 m.

Site 3 is located within the second marine terrace mIII₃₋₄, at 12 m asl, where drilling stripped a similar section consisting of clay silt with lens-like and layered cryostructures (10 m); massive sand from 10 m to 25–35 m, and massive clay silt to 50 m.

Sites 4 and 5 lie within the first marine terrace (mIII–IV) at 10–12 m asl. The section observed in test boreholes is composed of clay silt, mainly with lens-like and layered cryostructures (5–8 m), massive sand (to 12–15 m), and clay silt (to at least 50 m) with massive or lens-like cryostructures and with rare intercalations of sand and silt. Data from geotechnical boreholes reveal downward increase in soil salinity within 13 m and highly saline soil below 4–8 m.

Site 6 is located in the Siliyakha River floodplain, at 2 m asl. The section of geotechnical boreholes is composed of clay silt and silt (13 m), with different ice contents and salinity increasing depthward, and cryopegs at depths of 7–10 m.

ERT surveys imaged the subsurface to a depth of 50 m.

ERT method

2D resistivity imaging was performed by the roll-along method (successive change of electrodes with overlaps) using a Geotech Logis *Omega-48* system [<http://www.geotech.ru>] consisting of three electrodes configured as Amn + mnB and spaced at 5 m; the total cable length was 212.5 m. The number and lengths of profiles were varied according to the size of the sites: short profiles for sites within 720 m and long profiles for those within 1680 m. The profiles were 50 m apart.

ERT results

The acquired ERT data were prepared and pre-processed with the *X2IPI* software designed by A. Bobachev [<http://x2ipi.ru>] and inverted in *Zond-Res2D* [Kaminskiy et al., 2016]. The results of 2D inversion and their interpolation were used for resistivity mapping.

The resistivity patterns of selected sites were presented as histograms of inverted ERT data and as typical vertical electric sounding (VES) curves. The histograms were made with an assumption of lognormal resistivity distribution (Fig. 2) and equal widths of intervals in logarithmic coordinates.

All resistivity sections have a layered general structure (without regard to seasonal thaw).

Site 1: resistivity from 100 to 10 000 Ohm·m, with the main peak at 7000–9000 Ohm·m and a broad peak at 600–3000 Ohm·m. The typical VES curve shows gradual resistivity increase with depth in a three-layer section (type A). Inversion of ERT data from a typical section at site 1 reveals thin layers of lower resistivity (400–500 Ohm·m) in the near-surface (Fig. 2).

Site 2: resistivity in a range of 100–8000 Ohm·m, with peaks at 300–3000 and 6000–7000 Ohm·m. The VES curve is of K type (Fig. 2), with the most resistive middle layer in a three-layer section. ERT data show resistive rocks almost throughout the section, with local lows in the near-surface and locally with a conducting lower layer (~100 Ohm·m).

Site 3: resistivity from 100 to 9000 Ohm·m, with a prominent peak at 1000–2000 Ohm·m and a low peak of 200 Ohm·m. The VES curve is of K type (Fig. 2). The typical ERT section shows local shallow conductors among resistive rocks and a conducting lower layer of 100–200 Ohm·m.

Site 4: resistivity generally varying from 10 to 10 000 Ohm·m with prominent peaks of 60 and 600 Ohm·m. The VES curve is of a KH type (four layers, with the highest resistivity in the second layer and the lowest values in the third layer). A resistive layer of variable thickness with near-surface conductors lying over conductive rocks (~60 Ohm·m) and a low-resistivity lowermost layer (50–60 Ohm·m).

Site 5: resistivity variations mostly from 30 to 3000 Ohm·m, with several peaks at 60, 100–200 and 500–600 Ohm·m. H-type VES curve of a three-layer section with the lowest resistivity in the middle. ERT sections show horizontally uniform layers of high (600–2000 Ohm·m), low (60 Ohm·m), and quite low (100–200 Ohm·m) resistivity.

Site 6: a large resistivity range of 0.6 to 2000 Ohm·m with small peaks at 0.9–4 and 500–700 Ohm·m; H-type VES curve (Fig. 2); contrasting ERT section with a high-resistivity top layer, a conductor in the middle, and a resistive lowermost layer.

The sites can be tentatively divided into three groups according to resistivity patterns. Resistivity in ERT sections of type A fit a range of 100 to 10 000 Ohm·m (Fig. 2, *a–c*) and may have two prominent peaks in the histograms. This pattern corresponds to Upper Quaternary marine deposits of terraces III and II (see an example from site 1 in Fig. 3).

Type B sections show a larger resistivity range of 10 to 10 000 Ohm·m, with two prominent peaks and represent Upper Quaternary deposits of marine terrace I (site 5 in Fig. 4).

Type C includes sections with resistivity varying from 0.6 to 2000 Ohm·m, with two peaks, which are common to Holocene alluvium in the floodplain (see an example in Fig. 5). Note that the floodplain site partly lies within a dry lake (khasyrei), and the resistivity pattern reveals a seasonally freezing open talik that formed while the lake was filled with water.

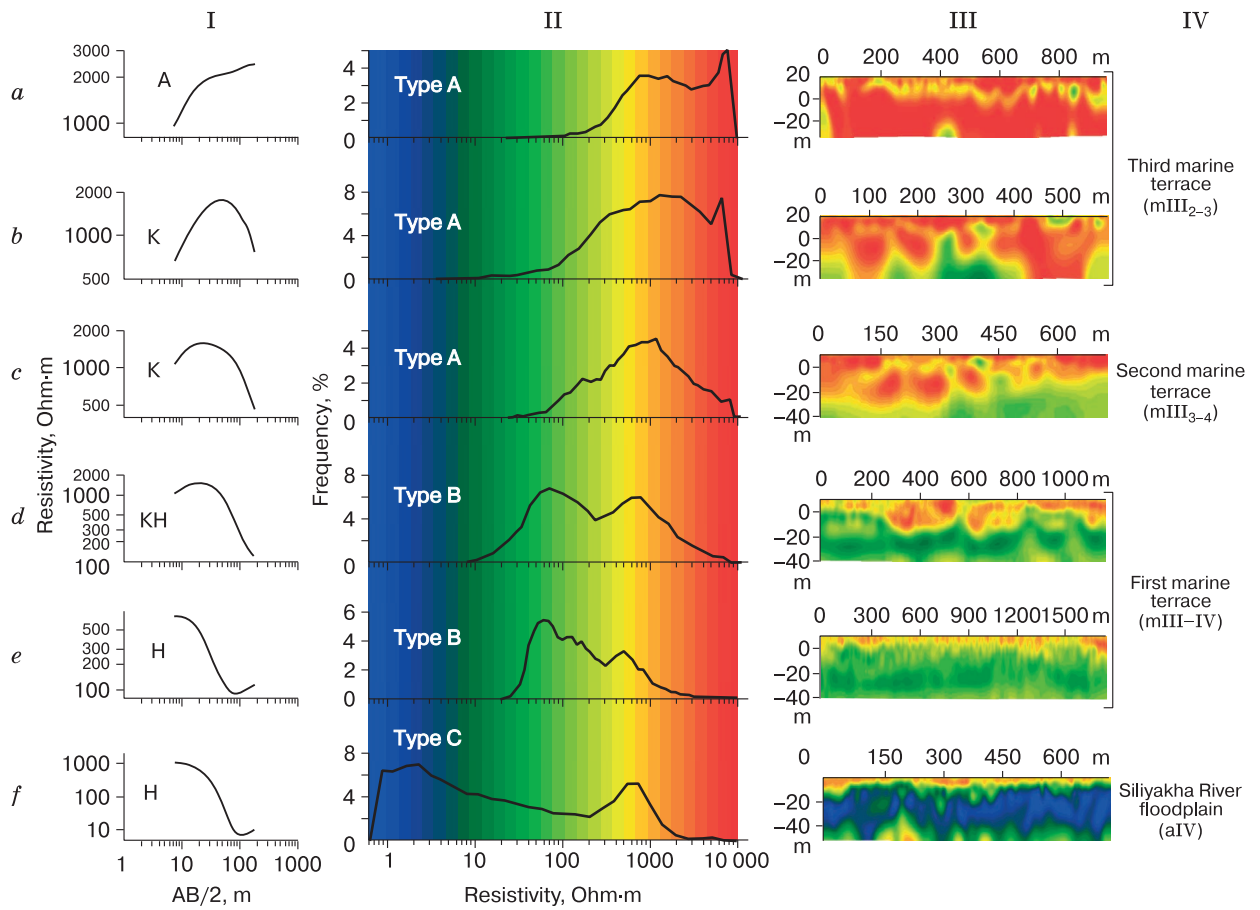


Fig. 2. Averaged VES curves (I), resistivity histograms (II), typical resistivity cross sections (III) according to ERT data, and assignment of surveys sites to geomorphological levels (IV).

a–f: sites 1–6, respectively. AB/2 – half spacing. The color codes are the same in all panels.

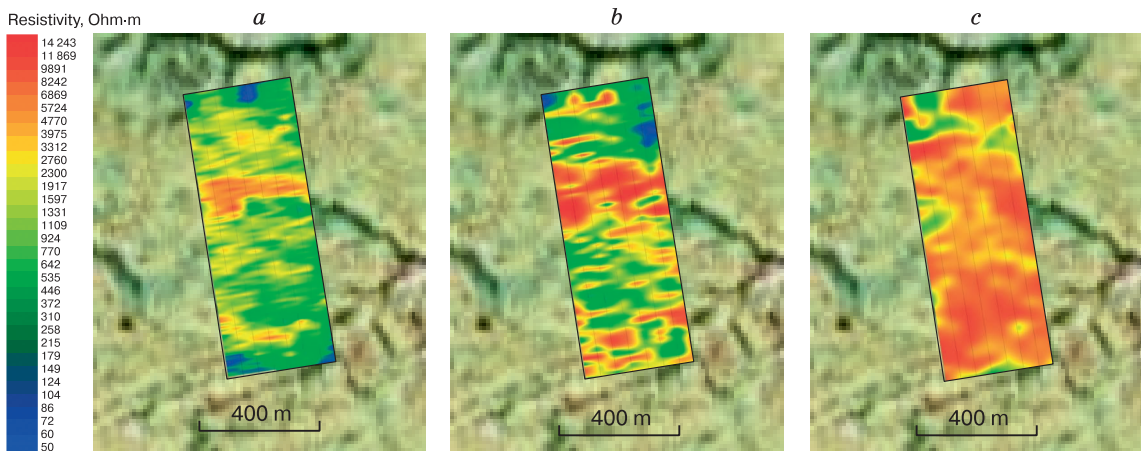


Fig. 3. Resistivity distribution at different depths, site 1.

a: 1.5 m; b: 6 m; c: 16 m.

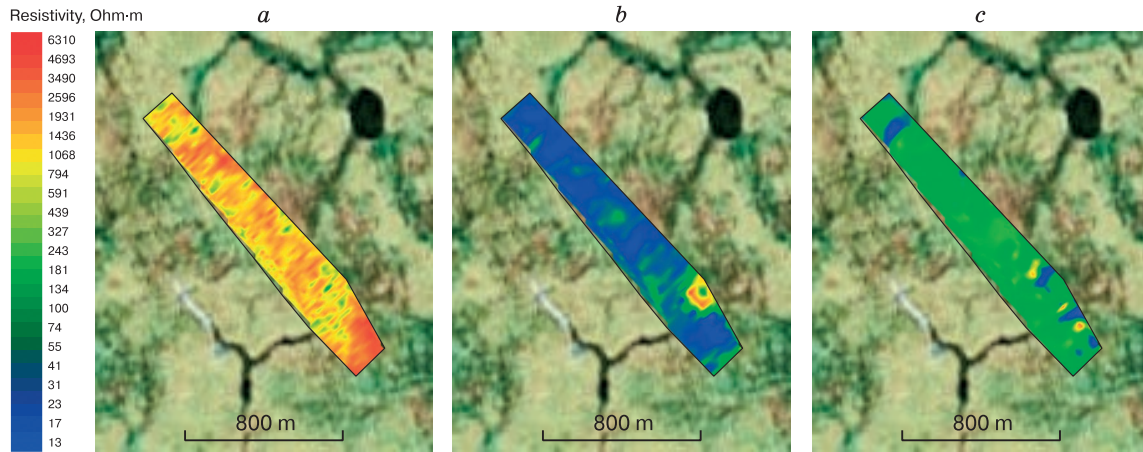


Fig. 4. Resistivity distribution at different depths, site 5.

a: 3 m; b: 24 m; c: 54 m.

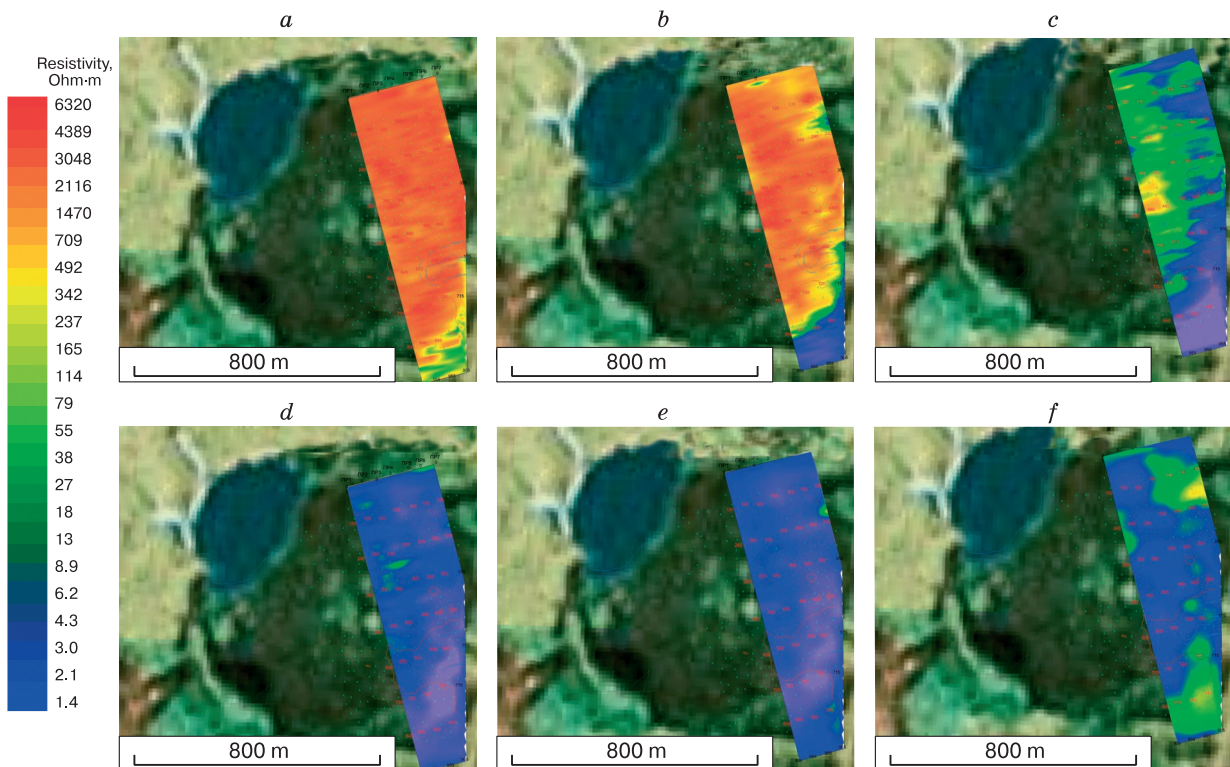


Fig. 5. Resistivity distribution at different depths, site 6.

a: 2 m; b: 5 m; c: 10 m; d: 15 m; e: 20 m; f: 35 m.

Resistivity modeling from physical properties of soil

Inversion with the *PetroWin* software (designed by A. Ryzhov) allows estimating the resistivity of a two-component sand-clay mixture with reference to its known water contents and physical properties [Matveev and Ryzhov, 2006].

Rocks with saline pore fluids have lower freezing temperatures and contain free unfrozen water [Yakupov, 2008]. The conductivity of frozen ground depends on pore fluid salinity [Dakhnov, 1953]. Resistivity of the sand-clay samples was calculated taking into account their temperature, sizes of clay and sand particles, cation-exchange capacity of clay, water con-

Table 1. Properties of samples

Number	Sample characteristics	D_{sal}	W_{tot}	n	I_{tot}	UWC
1	Frozen clay, high ice content, zero salinity	0.11	60	69	59	1
2	Frozen clay silt, high ice content, zero salinity	0.09	61	71	60	1
3	Frozen clay silt, zero salinity	0.12	47	58	43	4
4	Frozen clay silt, low ice content, zero salinity	0.11	33	50	28	5
5	Frozen clay, medium ice content, low salinity	0.20	50	57	44	6
6	Frozen clay, low ice content, zero salinity	0.17	43	50	35	8
7	Frozen clay, medium ice content, low salinity	0.36	50	57	40	10
8	Frozen clay, low ice content, low salinity	0.29	43	50	30	13
9	Frozen clay, medium ice content, medium-saline	0.53	48	65	32	16
10	Frozen clay, low ice content, medium salinity	0.52	45	51	24	21
11	Frozen silt, low ice content, medium salinity	0.41	37	44	10	27
12	Frozen silt, low ice content, medium salinity	0.36	37	44	14	23
13	Frozen clay, zero ice content, low salinity	0.32	37	43	16	21
14	Frozen clay, low ice content, low salinity	0.29	43	50	30	13
15	Frozen clay, low ice content, low salinity	0.29	43	50	30	13
16	Frozen clay, medium ice content, zero salinity	0.18	49	59	44	5
17	Frozen clay silt, low ice content, zero salinity	0.11	42	50	36	5
18	Frozen clay, medium ice content, zero salinity	0.12	49	59	46	3
19	Frozen clay, high ice content, zero salinity	0.15	60	69	58	2
20	Frozen clay silt, medium ice content, zero salinity	0.05	47	58	45.5	1.5
21	Frozen clay silt, high ice content, zero salinity	0.11	62	73	61	1
22	Frozen clay silt, very high ice content, zero salinity	0.12	70	79	69	1
23	Frozen silt, low ice content, zero salinity	0.08	39	46	37	2
24	Frozen clay silt, high ice content, low salinity	0.20	60	68	57	3
25	Frozen clay silt, medium ice content, zero salinity	0.12	47	58	45	2
26	Frozen clay silt, low ice content, zero salinity	0.11	41	50	36	5
27	Frozen clay silt, medium ice content, low salinity	0.28	51	60	44	7
28	Frozen clay, low ice content, low salinity	0.29	34	50	21	13
29	Frozen clay silt, medium ice content, medium salinity	0.57	48	55	31	17
30	Frozen clay silt, low ice content, low salinity	0.28	41	48	26	15
31	Frozen clay silt, low ice content, medium salinity	0.76	41	47	1	40
32	Frozen clay silt, low ice content, high salinity	0.99	44	48	1	43
33	Very soft clay silt	–	44	44	–	–
34	Frozen silty sand, medium ice content, zero salinity	0.03	39	43	37	2
35	Frozen sand, medium ice content, low salinity	0.06	40	47	37	3
36	Frozen silty sand, medium ice content, low salinity	0.09	39	44	33	6
37	Frozen silty sand, medium ice content, low salinity	0.10	34	42	27	7
38	Frozen silty sand, medium ice content, medium salinity	0.19	39	44	28	11
39	Frozen silty sand, low ice content, medium salinity	0.19	33	43	19	14
40	Frozen silty sand, medium ice content, high salinity	0.64	42	46	9	33
41	Silty sand	–	37	40	–	–

Note: D_{sal} = salinity degree, %; W_{tot} = total water content, vol.%; n = porosity, vol.%; I_{tot} = total ice content, vol.%; UWC = unfrozen water content, vol.%.

tent, and porosity, as well as salinity and volumetric fraction of pore fluids.

According to *a priori* data provided by the client and to published evidence [Badu *et al.*, 2006; Badu, 2015], the permafrost temperatures at the ERT survey sites are mostly within -4 to -5.5 °C (except for the upper 5 m). The available data for sites 4–6 including porosity, salinity, total water and ice con-

tents, soil skeleton density, and volumetric fraction of pore water (Table 1) were used to calculate theoretical resistivity-salinity NaCl (C_{ps} , g/L) relationships for the respective samples (Fig. 6).

Resistivities (ρ , Ohm·m) were calculated from volumetric percentages of pore fluids for selected samples. Thus a set of 41 points was obtained and then approximated by the previously suggested

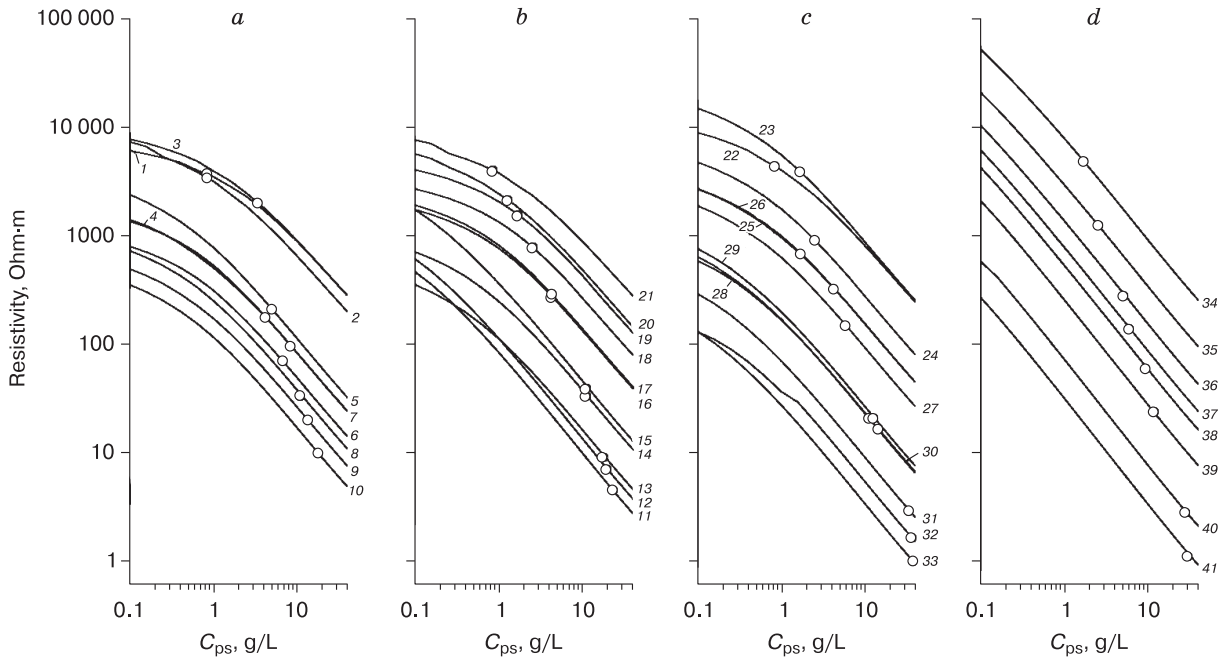


Fig. 6. Theoretical salinity (C_{ps}) dependence of resistivity for samples from sites 4–6.

a: site 5; *b*: site 4; *c*: site 6; *d*: sites 4, 6. Points on curves are calculated resistivities for samples at a fixed amount of pore fluid, 1–41 are sample numbers from Table 1.

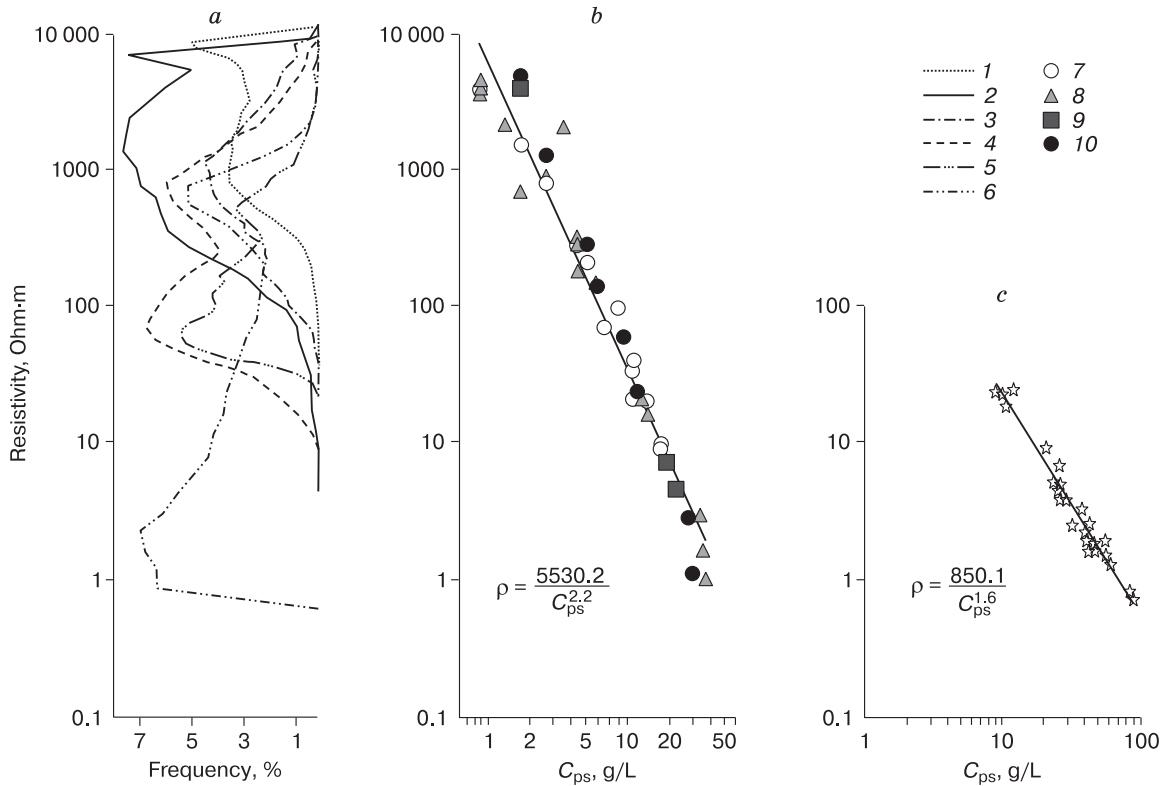


Fig. 7. *a*: Resistivity histograms at six ERT sites; *b*: resistivities calculated using Zykov's equation; *c*: Zykov's data on Na-Cl-saturated samples from Yamal at -5°C and their approximation by the respective equation (solid line).

1–6 = sites 1–6; 7 = clay, 8 = clay silt, 9 = silt, 10 = sand.

[Zykov, 2007] universal relationship $\rho = A/C_{ps}^b$ with the coefficients $A = 1400$ and $b = 1.85$ at -5°C . Our data from sites 4–6 fitted the best the approximation with $A = 5530.2$ and $b = 2.2$ (Fig. 7). This relationship differs from that for clay silt and sand samples from the Yamal Peninsula reported by Zykov [2007], where the coefficients are $A = 850.1$ and $b = 1.6$. The difference is due to local features and different sampling depths. Therefore, the equation requires calibration in accordance with the current local physical and geological features.

The resistivity histograms of Fig. 7 used for correlation with the chosen resistivity-salinity relationship generally cover all resistivity values obtained from ERT. The low-salinity domain mainly includes samples with high total ice contents (Figs. 6, 7; Table 1). Samples with salinities 30–40 g/L correspond to cold rocks at two points (33 and 41). The set of samples grouped according to ice and water contents and salinity is sufficient for correlation with the resistivity histograms. Further on, the relationship $\rho = 5530.2/C_{ps}^{2.2}$ is applied to all ERT sites.

The coefficients obtained for sites 4–6 can be used to estimate salinity of pore fluids till the depths resolvable by ERT (50 m). With the equation $C_{ps} = (5530.2/\rho)^{0.45}$, the resistivity-depth profiles can be converted to those of salinity (Fig. 8). Thus, ERT allows interpolation of properties known from geotechnical boreholes (depths to 13 m) and extrapolation to a depth of 50 m.

The obtained salinity patterns (Fig. 8) correlated to resistivity are heterogeneous. Generally, the salinity at the sites of type A does not exceed 3 g/L in the upper section and reaches 8–10 g/L in the lower part. The type-B sites have salinities of 6 g/L in the upper part, 10–11 g/L in the middle, and again 6 g/L locally in the lower layer. According to data from geotechnical boreholes, salinity increases gradually with depth from the section top, and highly saline soils appear from the depths 4–8 m. The transition to highly saline soils coincides with the gradient of salinity changes according to ERT. Sites of type B consist of a thin low-salinity near-surface layer lying over a high-salinity layer (to 40 g/L, locally to 45–50 g/L). Geotechnical borehole data show depthward salinity increase and the presence of cryopegs at 7–10 m. Then the salinity decreases again to 10–20 g/L in the lower section.

The resistivity of saline soils is known to depend more on salinity than on lithology [Zykov, 2007], which is consistent with the resistivity modeling results (Figs. 6, 7; Table 1). Thus, ERT is inapplicable for lithological division of these soils.

CONCLUSIONS

ERT surveys in the area of the Kharasavei gas and condensate field reveals resistivity variations in a

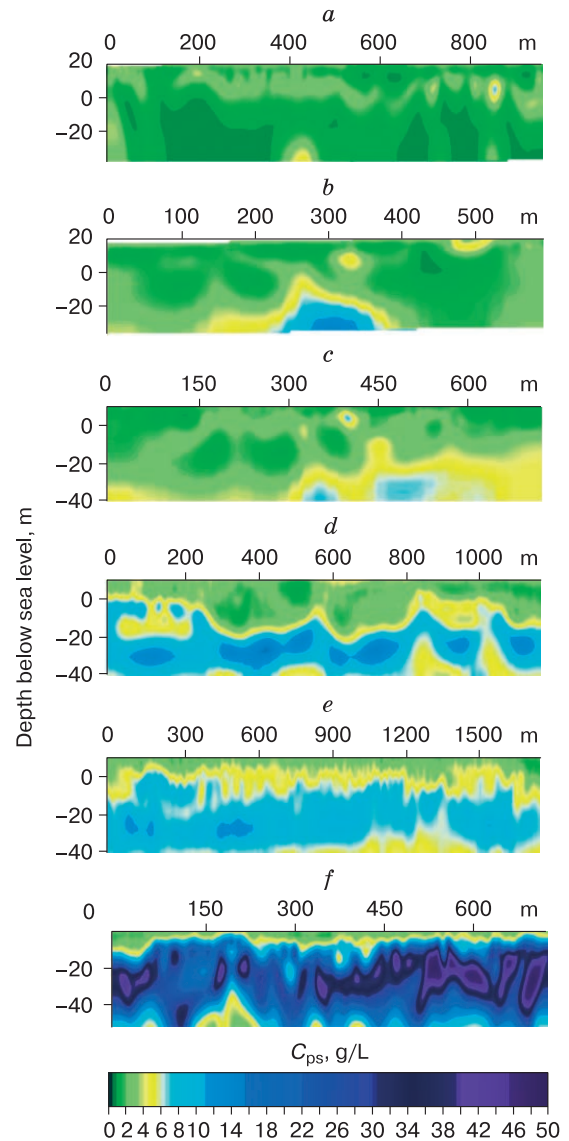


Fig. 8. Pore fluid salinity calculated from resistivity data using the equation $C_{ps} = (5530.2/\rho)^{0.45}$.

a: site 1, type A; b: site 2, type A; c: site 3, type A; d: site 4, type B; e: site 5, type B; f: site 6, type C.

large range from 0.6 to 10 000 Ohm·m in the shallow subsurface.

The sites located in the second and third marine terraces have been grouped according to the ranges and absolute values of resistivity presented in histograms and correlated with geomorphic conditions. Generally, the resistivity range covers two orders of magnitude, from 100 to 10 000 Ohm·m, with two peaks. The range is as large as 10 to 10 000 Ohm·m at sites in the first marine terrace, with two modes, but is from 0.6 to 2000 Ohm·m at the site in the Siliyakha River floodplain, likewise with two largely spaced

modes: a distribution presumably controlled by the presence of cryopegs.

The shallow resistivity patterns within the Kharasavei field can be approximated by the relationship $\rho = A/C_{ps}^b$ [Zykov, 2007]. Modeling of soil physical properties jointly with inversion of ERT data allowed estimating the coefficients in the Zykov equation as $A = 5530.2$ and $b = 2.2$ at rock temperatures from -4 to -5.5 °C for various lithologies from clay and clay silt to silt and sand.

With the obtained salinity dependence of resistivity, it became possible to convert resistivity to salinity at the sites within certain geomorphological levels of the Kharasavei gas and condensate field.

Thus estimated pore fluid salinity has implications for the thermal state of permafrost, operation of geotechnical facilities, and properties of saline rocks.

References

- Badu, Yu.B., 2015. Ice content of cryogenic strata (permafrost interval) in gas-bearing structures, Northern Yamal. *Earth's Cryosphere* XIX (3), 9–18.
- Badu, Yu.B., Podbornyi, E.E., 2006. Division of permafrost according to cryostratigraphy and complexity of geocryological conditions, with implications for drilling and operation of wells. In: *Permafrost of Oil-Gas-Condensate Fields in the Yamal Peninsula*. Nedra, Saint Petersburg, vol. 1, pp. 289–300. (in Russian)
- Badu, Yu.B., Vasil'chuk, Yu.K., Podbornyi, E.E., 2006. Distribution and temperatures of permafrost. In: *Permafrost of Oil-Gas-Condensate Fields in the Yamal Peninsula*. Nedra, Saint Petersburg, vol. 1, pp. 84–89. (in Russian)
- Budantseva, N.A., Badu, Yu.B., Vasil'chuk, Yu.K., Podbornyi, E.E., 2006. Salinity of soils. In: *Permafrost of Oil-Gas-Condensate Fields in the Yamal Peninsula*. Nedra, Saint Petersburg, vol. 1, pp. 145–167. (in Russian)
- Dafflon, B., Hubbard, S., Ulrich, C., et al., 2016. Geophysical estimation of shallow permafrost distribution and properties in an ice-wedge polygon-dominated Arctic tundra region. *Geophysics* 81, pp. WA247–WA263.
- Dakhnov, N.V., 1953. *Resistivity Surveys in Oil and Gas Fields*. Gostoptekhizdat, Moscow, 692 pp. (in Russian)
- Hauck, C., 2002. Frozen ground monitoring using DC resistivity tomography. *Geophys. Res. Lett.* 29 (21), 1–4.
- Hubbard, S.S., Gangodagamage, C., Dafflon, B., et al., 2013. Quantifying and relating land-surface and subsurface variability in permafrost environments using LiDAR and surface geophysical datasets. *Hydrogeology J.* 21, 149–169.
- Ingeman-Nielsen, T., Foged, N., Butzbach, R., Jørgensen, A.S., 2008. Geophysical investigation of saline permafrost at Illulissat, Greenland. In: *Proc. of the Ninth Intern. Conf. on Permafrost*, Fairbanks, USA, University of Alaska, vol. 1, pp. 773–778.
- Kaminskiy, A.E., Erokhin, S.A., Politcina, A.V., 2016. Full inversion of shallow geophysical data. *Inzhenernye Izyskaniya*, No. 9, 44–51.
- Krautblatter, M., Verleysdonk, S., Flores-Orozco, A., Kemna, A., 2010. Temperature-calibrated imaging of seasonal changes in permafrost rock walls by quantitative electrical resistivity tomography (Zugspitze, German/Austrian Alps). *J. Geophys. Res.: Earth Surface* 115 (F2), 1–15.
- Matveev, V.S., Ryzhov, A.A., 2006. Geophysical support for regional hydrogeological, engineering-geological, geocryological, and geoenvironment studies. *Razvedka i Okhrana Nedr*, No. 2, 50–57.
- Oldenborger, G.A., LeBlanc, A.-M., 2017. Time-lapse electrical resistivity surveys and unfrozen water content in cold continuous permafrost. In: *Proc. of the 17th Near Surface Geosci. Conf., EAGE (3–7 Sept. 2017)*, Malmo, Sweden, Tu 23 B11, pp. 1–5.
- Olenchenko, V.V., Sinitsky, A.I., Antonov, E.Y., Eltsov, I.N., Kushnarenko, O.N., Plotnikov, A.E., Potapov, V.V., Epov, M.I., 2015. Results of geophysical surveys of the area of “Yamal crater”, a new geological structure. *Earth's Cryosphere* XIX (4), 84–95.
- Podbornyi, E.E., 2006. Geomorphological characteristic. In: *Permafrost of Oil-Gas-Condensate Fields in the Yamal Peninsula*. Nedra, Saint Petersburg, vol. 1, pp. 38–48. (in Russian)
- URL: <http://www.geotech.ru> (last visited 01.05.2011).
- URL: <http://x2ipi.ru> (last visited 01.09.2013).
- Yakupov, V.S., 2008. *Geophysics of Permafrost Areas*. Yakutsk University Press, Yakutsk, 342 pp. (in Russian)
- Yoshikawa, K., Leuschen, C., Ikeda, A., et al., 2006. Comparison of geophysical investigations for detection of massive ground ice (pingo ice). *J. Geophys. Res.: Planets* 111 (E06S19), 1–10.
- Zykov, Yu.D., 2007. *Geophysical Surveys in Permafrost*. Moscow University Press, Moscow, 272 pp. (in Russian)

Received December 27, 2016

Revised version received November 10, 2019

Accepted January 22, 2019